

# Multi-frequency Observations of the Radio Galaxy 4C 26.42 and Diffuse Radio Emission in the Galaxy Cluster A1795



A thesis submitted towards partial fulfilment of  
BS-MS Dual Degree Programme

by

SREE VANI JARUGULA

under the guidance of


DR. K.S.DWARAKANATH

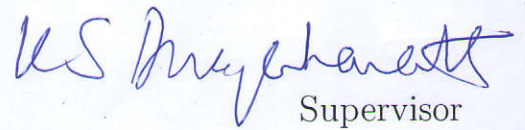
RAMAN RESEARCH INSTITUTE

INDIAN INSTITUTE OF SCIENCE EDUCATION AND RESEARCH PUNE

# Certificate

This is to certify that this thesis entitled "Multi-frequency Observations of the Radio Galaxy 4C 26.42 and Diffuse Radio Emission in the Galaxy Cluster A1795" submitted towards the partial fulfilment of the BS-MS dual degree programme at the Indian Institute of Science Education and Research Pune represents original research carried out by Sree Vani Jarugula at Raman Research Institute, under the supervision of Prof. K.S.Dwarakanath during the academic year 2014-2015.

Student   
SREE VANI JARUGULA

  
Supervisor

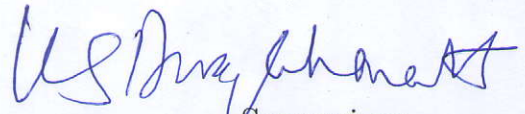
K.S.DWARAKANATH

# Declaration

I hereby declare that the matter embodied in the report entitled "Multi-frequency Observations of the Radio Galaxy 4C 26.42 and Diffuse Radio Emission in the Galaxy Cluster A1795" are the results of the investigations carried out by me at the Department of Astronomy and Astrophysics, Raman Research Institute, under the supervision of Prof. K.S.Dwarakanath and the same has not been submitted elsewhere for any other degree.

Student

  
SREE VANI JARUGULA

  
Supervisor

K.S.DWARAKANATH

# Acknowledgements

First and foremost I would like to thank Prof. K.S. Dwarakanath, my thesis advisor, for his invaluable time, patience and guidance without which this wouldn't have been possible. I am extremely grateful to him for motivating me and making me believe in myself. His guidance helped me in better understanding of the subject. *Sir, thank you.*

I am also thankful to Ruta Kale for not only flagging and calibrating the data, but also for helping me out with AIPS. I am grateful for her patient replies to my queries.

I would also like to thank Prof. Ramana Athreya for his valuable suggestions and for his time and Prof. Nissim Kanekar for his support. I am thankful to my family especially my sister, Sree Lekha and my friends, Abhijith and Anil for being with me throughout.

I am grateful to the office staff of Raman Research Institute especially Vidya ma'am for providing me with office space and for guiding me through the formalities. I would also like to thank the canteen staff of RRI for the timely coffee.

I am grateful to Indian Institute of Science Education and Research, Pune for giving me an opportunity to do my thesis work at Raman Research Institute.

# Abstract

We have observed the galaxy cluster Abell 1795 at 610  $MHz$  and 235  $MHz$  using the Giant Metrewave Radio Telescope (GMRT). Abell 1795 (A1795) is a relaxed cluster at a redshift of 0.06 and hosts a bright galaxy, 4C 26.42 in the centre. The motivation behind this thesis work is two fold: to confirm the presence of a mini-halo that is claimed to be present in the core of the galaxy cluster A1795 and to analyse the spectrum of the Brightest Cluster Galaxy (BCG), 4C 26.42. It is interesting to study mini-halos (diffuse radio emission of extent  $\sim 100 kpc$ ) in galaxy clusters because the spectrum of mini-halo can give information on the properties of the intracluster medium and on the evolution of the galaxy cluster. Till date only 21 mini-halos have been detected. Hence, it becomes important to detect more mini-halos to understand their spectra, properties and origin. Similarly, the spectrum of a galaxy is studied to understand the energetics and the lifetime of the galaxy. BCGs are massive galaxies at the centre of galaxy clusters and are most likely to host Active Galactic Nuclei. It is therefore interesting to study the spectrum of BCGs.

Mini-halos are diffuse radio sources in the centre of a relaxed galaxy cluster. This diffuse non-thermal radio emission is due to synchrotron radiation of the relativistic electrons in the intracluster medium. A possible detection of a mini-halo in this cluster at 1.4  $GHz$  with a flux density of  $85 \pm 5 mJy$  has been claimed. To confirm its presence, we analysed GMRT observations of A1795 at 610  $MHz$  and 235  $MHz$  using Astronomical Image Processing System (AIPS). Radio spectrum of the form  $S_\nu \propto \nu^{-\alpha}$  where  $S_\nu$  is the flux density at frequency  $\nu$  and  $\alpha$  is the spectral index is considered. Given the flux density of the mini-halo at 1.4  $GHz$ , a flux density of atleast 160  $mJy$  at 610  $MHz$  is expected by considering  $\alpha = 1$ . However, from a  $2'$  by  $2'$  region ( $\sim 100 kpc$  in linear scale, the typical size of a mini-halo) around the central galaxy in the image containing only diffuse emission, we detected a flux density of  $\sim 18 mJy$  at 610  $MHz$  which is a factor of  $\sim 10$  less than expected. We therefore give an upper limit of 18  $mJy$  for the detection of the mini-halo in this cluster.

We analysed the Brightest Cluster Galaxy (BCG) 4C 26.42 in the galaxy cluster A1795 at 610  $MHz$  and 235  $MHz$ . Using the flux density values of this galaxy from literature, we obtained the spectrum from 74  $MHz$  to 43.34  $GHz$  at 8 frequencies. The spectrum follows the least square fit:  $\log S_\nu = -0.14(\log \nu)^2 - 0.16(\log \nu) + 4.8$ . In order to estimate the break frequency, we fit two curves of the form  $S_\nu \propto \nu^{-\alpha}$ . The spectral indices from the least square fits are:  $\alpha_{74MHz}^{1.4GHz} \equiv \alpha_1 = 0.83 \pm 0.05$  and  $\alpha_{4.86GHz}^{43.34GHz} \equiv \alpha_2 = 1.37 \pm 0.14$ . The break frequency is  $\sim 2GHz$ .  $\alpha_2 \sim \alpha_1 + 0.5$  which is as expected from the spectral aging models before and after the break frequency. Assuming equipartition of energy between the particle energy density and the magnetic field energy, we estimated the magnetic field strength and the energy of the relativistic electrons to be  $\sim 36 \mu G$  and  $\sim 8 \times 10^{56} \text{ erg}$  respectively. Using the break frequency and the magnetic field, the age of relativistic electrons in the galaxy is estimated to be  $\sim 3.4 \text{ Myr}$ . The spectral indices of the various components of this galaxy have previously been studied at the parsec scale. In this thesis, we discuss the spectrum of the galaxy as a whole (at the kilo parsec scale).

# Contents

<b>1</b>	<b>Introduction</b>	<b>5</b>
1.1	Galaxy Clusters . . . . .	5
1.2	Intra Cluster Medium . . . . .	6
1.2.1	Thermal and Non-Thermal Components . . . . .	6
1.3	Diffuse radio emission . . . . .	8
1.3.1	Synchrotron Emission . . . . .	8
1.3.2	Inverse Compton Scattering . . . . .	9
1.4	Spectral Aging Models . . . . .	10
1.5	Cool Cores and Cold Fronts . . . . .	13
1.6	A1795 . . . . .	14
1.6.1	4C 26.42 . . . . .	14
1.7	Motivation . . . . .	14
<b>2</b>	<b>Observations</b>	<b>17</b>
2.1	Radio Telescope . . . . .	17
2.2	Radio Interferometry . . . . .	19
2.3	GMRT . . . . .	20
2.4	Observations at 610 MHz and 235 MHz . . . . .	21
<b>3</b>	<b>Data Analysis</b>	<b>23</b>
3.1	Flagging and Calibration . . . . .	23
3.2	Imaging . . . . .	25
3.2.1	CLEAN algorithm . . . . .	27
3.2.2	Weighting . . . . .	28
3.2.3	Polyhedron Imaging . . . . .	30

3.2.4	610 MHz . . . . .	31
3.2.5	235 MHz . . . . .	32
<b>4</b>	<b>Results</b>	<b>34</b>
4.1	Radio Images of BCG . . . . .	34
4.1.1	610 MHz . . . . .	34
4.1.2	235 MHz . . . . .	35
4.2	Spectrum of BCG . . . . .	35
4.3	Break frequency . . . . .	36
4.4	Magnetic field from Equipartition of Energy . . . . .	37
4.5	Age of relativistic electrons . . . . .	40
<b>5</b>	<b>Discussion</b>	<b>42</b>
5.1	Diffuse Emission . . . . .	42
5.1.1	Upper limit on flux density of mini-halo . . . . .	42
5.1.2	Radio Power of mini-halo at 1.4 GHz . . . . .	43
5.1.3	Implications . . . . .	45
5.2	Brightest Cluster Galaxy . . . . .	46
5.2.1	Magnetic field and Total Energy . . . . .	46
5.2.2	Spectrum . . . . .	48
5.2.3	Implications . . . . .	48
	<b>References</b>	<b>50</b>



# Chapter 1

## Introduction

### 1.1 Galaxy Clusters

Galaxy clusters are the largest structures in the universe which are gravitationally bound. A galaxy cluster contains tens to hundreds of galaxies with typical masses of  $\sim 10^{15} M_{\odot}$  and extends to  $\sim 100 Mpc^3$  ( $1 pc = 3.1 \times 10^{16} m$ ). From the study of velocities of galaxies and gravitational lensing effects, it has been observed that about 80% of mass of a galaxy cluster consists of dark matter. The total mass of galaxies is 3-5% of the total cluster mass. The rest 15-17% is made up of hot low dense plasma ( $\sim 10^8 K$  and  $10^{-3} atoms/cm^3$ ) called the intra cluster medium (ICM).

Galaxy clusters follow the hierarchical structure formation through accretion of small clusters and groups. The denser regions form a filamentary structure in the universe and galaxy clusters are formed in and usually at the intersections of these filaments. As the matter is accreted, the gas is heated to very high temperatures of  $\sim 10^8 - 10^9 K$  due to infall. This gas eventually reaches hydrostatic equilibrium and settles in the cluster potential. As the density of the gas increases, the cooling rate increases which leads to formation of stars and super massive blackholes in the cluster galaxies. The formation of stars and massive blackholes further lead to supernovae and AGNs which again heat the intra cluster medium (ICM).

## 1.2 Intra Cluster Medium

The Intra Cluster Medium (ICM) is made up of diffuse low density ( $10^{-3}$  atoms/cm<sup>3</sup>) hot plasma  $\sim 10^8$  K and contains large scale magnetic fields of the order of  $\sim 0.1 - 1$   $\mu$ G which is detected by rotation measures. In ICM, the thermal components are mixed with the non-thermal components.

### 1.2.1 Thermal and Non-Thermal Components

The high temperatures in ICM result in X-ray emission due thermal bremsstrahlung. The ICM also consists of non-thermal components which can be detected at radio wavelengths. Non-thermal emission is due to synchrotron emission from relativistic electrons. These non-thermal components extend to hundreds of kilo parsec and are associated with the ICM and not the individual radio galaxies. The time taken for electrons to travel from the radio galaxy across the diffuse radio emission region is much longer than the radiative lifetime of the electron itself which is  $10^7$ - $10^8$  years for  $\gamma = 10^4$ . To explain this diffuse radio emission, it is proposed that relativistic electrons are accelerated insitu in ICM due to turbulence or shock waves generated during merger activity. The radio emission due to synchrotron radiation in ICM indicates the presence of large scale magnetic fields. The non-thermal components are classified as follows:

#### Halos

Halos are diffuse radio sources which are detected in merging clusters in the central regions of the galaxy cluster. They extend to sizes of the order 1 *Mpc*. Halos are unpolarized with low surface brightness ( $1-0.1 \mu$ Jy/arcsec<sup>2</sup> at 1.4 *GHz*). Their radio spectrum ( $S_\nu \propto \nu^{-\alpha}$ ) is steep and the spectral index  $\alpha$  is usually  $\geq 1$ . It is observed that the radio power of the halo at 1.4 *GHz* ( $P_{1.4}$ ) is correlated to the X-ray luminosity ( $L_X$ ) in merging clusters as  $P_{1.4} \propto L_X^2$  [7].

#### Relics

Relics are diffuse radio sources found in both merging and cool-core clusters. They extend to sizes of the order of 1 *Mpc*. Relics can be elongated or regular and roundish. The elongated relics are found at the periphery of clusters roughly perpendicular to the

cluster merger axis and lack any sub structures. The roundish and regular structured relics are found off the cluster centre and have filamentary substructures. Relics have a steep spectrum ( $\alpha \geq 1$ ) and are polarized to 20-30%. The radio power and X-ray luminosity of both elongated and roundish relics are correlated as  $P_{1.4} \propto L_X^{1.2}$  [7].

### Mini-halos

Mini-halos are the diffuse radio sources usually found in relaxed cool core galaxy clusters. Cool core clusters are clusters with a core which has a higher density and lower temperature than the surrounding ICM. Mini-halos extend to  $\sim 500$  kpc around the central radio galaxy and have steep spectrum ( $\alpha \geq 1$ ) with low surface brightness. Mini-halos can be distinguished from other steep spectrum sources like radio bubbles and AGN lobes from the fact that mini-halo emission is mixed with the X-ray emission while AGN lobes create cavities in X-ray emission. Mini-halos are difficult to detect given their proximity to a bright galaxy [7].

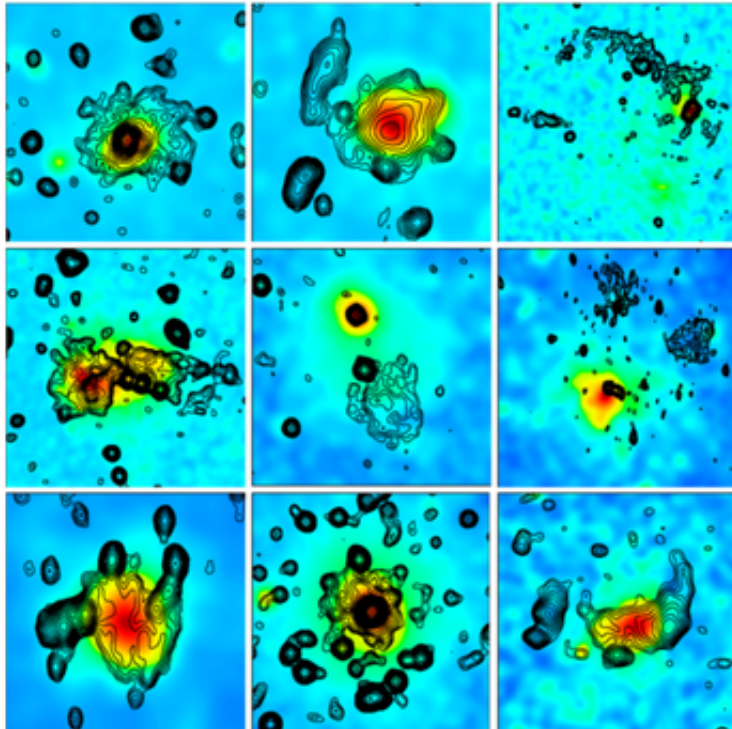


Figure 1.1: *Diffuse Radio Sources*

*The contours of diffuse radio emission are overlaid on X-ray images(in colour). The clusters (from left to right and top to bottom) are A2219 (halo), A2744(halo+relic), A115(relic), A754(complex halo+relic), A1664(relic), A548b(relic), A520(halo), A2029(mini-halo) and RXCJ1314.4-2515(halo+double relics) [7].*

## 1.3 Diffuse radio emission

### 1.3.1 Synchrotron Emission

When a charged particle is accelerated to relativistic energies in the presence of magnetic fields, it emits synchrotron radiation which is a non-thermal emission [14]. The power (in C.G.S) emitted by a single electron due to synchrotron radiation is given by:

$$P \equiv \frac{dE}{dt} = \frac{4}{3}\sigma_T\gamma^2\beta^2cU_B \quad (1.1)$$

where:

$\gamma = E/m_e c^2$  is the Lorentz factor

$\sigma_T$  is Thomson cross section

$U_B = B^2/8\pi$  is the magnetic energy density

$\beta = v/c$

The synchrotron losses increase with increase in the energy of the electron which gives rise to a curvature in the spectrum. The synchrotron radiative lifetime  $\tau$  of a particle is given by:

$$\tau = \frac{E}{dE/dt} \propto E^{-1}B^{-2} \quad (1.2)$$

### Synchrotron Spectrum for a single electron

The spectrum of synchrotron radiation by a single electron is given as:

$$P(\omega) = \frac{\sqrt{3}}{2\pi} \frac{q^3 B \sin\alpha}{mc^2} F\left(\frac{\omega}{\omega_c}\right) \quad (1.3)$$

where  $B$  is the magnetic field,  $\alpha$  is the pitch angle and  $\omega_c$  is the critical frequency given by:

$$\omega_c \equiv \frac{3}{2}\gamma^3\omega_B \sin\alpha \quad (1.4)$$

Here  $\gamma$  is the lorentz factor and  $\omega_B = qB/mc\gamma$  is the gyration frequency.

The form of the function  $F(\omega/\omega_c)$  is given in Figure 1.2.

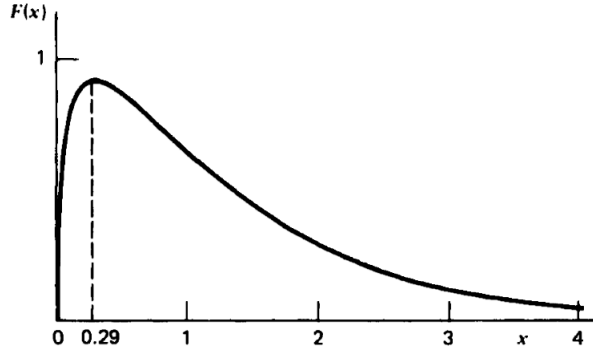


Figure 1.2: *The function describing the total power spectrum of synchrotron emission for a single electron. Here  $x \equiv \omega/\omega_c$  (Figure 6.6 from Rybicki and Lightman 1979) [14]*

### Synchrotron Spectrum for a powerlaw distribution of electrons

For a power law particle distribution given as  $N(\gamma)d\gamma = C\gamma^{-p}d\gamma$ , the total synchrotron power radiated is:

$$P_{tot}(\omega) = C \int_{\gamma_1}^{\gamma_2} P(\omega)\gamma^{-p}d\gamma \propto \int_{\gamma_1}^{\gamma_2} F\left(\frac{\omega}{\omega_c}\right)\gamma^{-p}d\gamma \quad (1.5)$$

Taking  $x \equiv \omega/\omega_c$ ,  $\omega_c \propto \gamma^2$  and approximating  $x_1 \approx 0$  and  $x_2 \approx \infty$  for sufficiently high energy limits, we get:

$$P_{tot}(\omega) \propto \omega^{-(p-1)/2} \quad (1.6)$$

This can be written as:

$$P_{tot}(\omega) \propto \omega^{-s} \quad (1.7)$$

Comparing this with synchrotron emission ( $S_\nu \propto \nu^{-\alpha}$ ), we see that  $\alpha \propto (p-1)/2$ .

Synchrotron self absorption at low frequencies can lead to a spectrum which follows  $S_\nu \propto \nu^{5/2}$  where  $\nu$  is the frequency. Through out this thesis we consider only Equation 1.7.

The detailed derivations can be found in Rybicki and Lightman, 1979 [14].

### 1.3.2 Inverse Compton Scattering

The inverse compton radiation takes place as photons are scattered off charged particles. The charged particles impart some of their energy to the photons which hence radiate at higher frequencies. In this thesis, we consider inverse compton scattering of the cosmic

microwave background (CMB) photons off the relativistic electrons which can lead to synchrotron radiation. The power is lost by the electron which is converted to radiation. This power is given by:

$$P \equiv \frac{dE}{dt} = \frac{4}{3} \sigma_T \gamma^2 \beta^2 c U_{CMB} \quad (1.8)$$

where  $U_{CMB}$  is the initial CMB photon energy.

The power radiated due to synchrotron radiation and inverse compton scattering is similar.

$$\frac{P_{Synch}}{P_{compton}} = \frac{U_B}{U_{CMB}} \quad (1.9)$$

Radiation due to inverse compton scattering depends upon the electric field in the electron's rest frame whereas synchrotron radiation is because of an accelerating electron in magnetic field.

The detailed derivations can be found in Rybicki and Lightman, 1979 [14].

## 1.4 Spectral Aging Models

From the theory of synchrotron emission,  $\nu \propto BE^2$  which shows that higher energy particles radiate at higher frequency. Since the synchrotron lifetime  $\tau \propto E^{-1}B^{-2}$ , particles with higher energy have lower radiative lifetimes. Hence, with time, the radio spectrum steepens at higher frequencies leading to a curved spectrum. The form of steepening depends on the changes in the distribution of the initial power law distribution of relativistic electrons, injection rate of the electrons and variation in the pitch angle distributions. Evolutionary models have been proposed taking these factors into consideration. Three basic and common models: the KP model proposed by Kardashev (1962) and Pacholczyk (1970), the JP model by Jaffe and Perola (1973) and the CI (Continuous Injection) model are discussed here [4].

### **KP model**

KP model considers one time injection of relativistic electrons. The initial electron distribution is isotropic and follows a power law. In KP model, the time-scale for continuous

isotropization of electrons is longer than the radiative lifetime of the electrons. Since synchrotron emission does not affect the pitch angle, the electrons maintain their original pitch angle. As seen from Equation 1.10, particles with higher pitch angle with respect to the magnetic field radiate faster. This leads to anisotropy in the distribution of the electrons which in turn affects the emission spectrum. The emission spectrum steepens above a certain break frequency and the slope of this new power law depends on the initial slope( $\alpha_{inj}$ ) of the injected power law as:

$$\alpha = \frac{4}{3}\alpha_{inj} + 1 \quad (1.10)$$

### **JP model**

The JP model considers isotropic one time injection of electrons which follow a power law. Unlike KP model, in JP model the time-scale for continuous isotropization of pitch angle is much smaller than the life time of electrons. This leads to a sharp cutoff in the electron distribution and an exponential cutoff in the emission spectrum.

### **CI model**

The CI model allows a continuous injection of electrons. In this model, the emission is from all the electrons having different ages: from the newly injected electrons to the electrons which were initially injected. The slope of the power law after the synchrotron break is related to the initial slope as:

$$\alpha = \alpha_{inj} + 0.5 \quad (1.11)$$

The spectral aging in the three models is shown in Figure 1.3.

### **The Komissarov and Gubanov Models (KG)**

The KGKP and KGJP models published by Komissarov and Gubanov (1994) assume continuous injection (CI) for a finite amount of time followed by a relic phase (RE) when the injection is stopped instead of a one time isotropic injection as proposed by KP and JP models. Synchrotron emission and inverse compton scattering of CMB photons take place during both CI and RE phases [15].

In KGKP model, three break frequencies occur:

$\nu_{br}$  is the break frequency in the first electron population which is injected in the beginning of CI phase.

$\nu'_{br}$  is the break frequency of the last electron population injected before the injection is stopped (beginning of RE phase)

$\nu''_{br}$  is due to inverse compton scattering of small pitch angle electrons.

The spectral indices are related as follows:

For  $\nu < \nu_{br}$ ,  $\alpha = \alpha_{inj}$

For  $\nu_{br} < \nu < \nu'_{br}$ ,  $\alpha = \alpha_{inj} + 0.5$

For  $\nu'_{br} < \nu < \nu''_{br}$ ,  $\alpha = \frac{4}{3}\alpha_{inj} + 1$

In KGJP, only two break frequencies  $\nu_{br}$  and  $\nu'_{br}$  occur because of isotropization of pitch angle. The spectral indices follow the same relations as given in KGKP model.

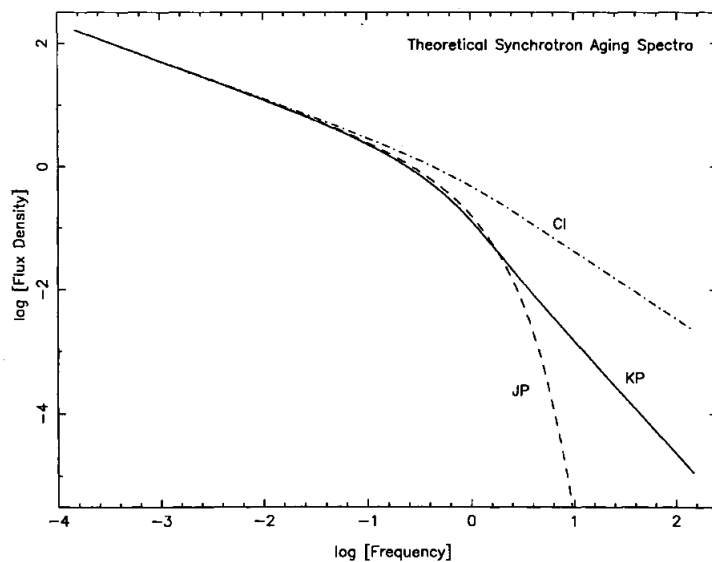


Figure 1.3: *Spectral Aging Models [4]*



## 1.5 Cool Cores and Cold Fronts

As the galaxies merge together to form clusters, they reach a relaxed state. The ICM in central region of the cluster becomes denser and the core of such a cluster is characterized by Brightest Cluster Galaxy (BCG) and strong X-ray emission. Because of the high densities, the gas in the centre has short radiative cooling times and hence enhanced X-ray emission. This led to the development of a cooling flow model where the cool gas is compressed by the surrounding gas and the hot gas flows in to replace this compressed gas. However, spectral studies revealed that the cooling rates from the cooling flow were over estimated. Heating mechanisms like conduction, AGN heating from BCG, heating due to shocks induced by AGN bubbles, etc are proposed to explain the discrepancy in the cooling rate. The “cooling flow” model is therefore replaced by “cool core”. A Cool core of a galaxy cluster has high density, high surface brightness and low temperature compared to the surrounding ICM.

Cold fronts in cool core clusters are sharp discontinuities in the density and temperature profiles with a rise in density (and hence surface brightness) and dip in gas temperature inside the cool core. Since the amplitude of changes in density and temperature are similar, the pressure across the cold front remains constant. Most of the galaxy clusters host at least one cold front. Cold fronts are formed either due to merger or non-merger activities.

### **Merger Cold Fronts**

Cold fronts arise due to merger events when the cold dense outermost gas of the merging subcluster is stripped followed by pressure exerted by the surrounding less dense gas leading to a contact discontinuity between the two systems [13].

### **Non-Merger Cold Fronts**

Cold fronts also arise during small mergers when the subcluster introduces a disturbance in the cool core. As the gas tries to get back to the minimum potential, a sloshing motion sets in leading to the formation of a cold front [8].

## 1.6 A1795

The Abell catalogue is a catalogue of about 4073 rich galaxy clusters at  $0.02 \leq z \leq 0.2$ . Abell published a catalogue of 2712 rich galaxy clusters for the Northern Sky in 1957 and the catalogue for the Southern Sky was included by Abell, Corwin and Olowin and published in 1989 [1]. Abell 1795 is a rich galaxy cluster at a redshift of about 0.06. This cluster is one of the most luminous clusters with a X-luminosity of  $\sim 8.5 \times 10^{44} \text{ ergs}^{-1}$  in the 0.5–4.5 keV band. The X-ray studies show that A1795 is a relaxed cool core cluster.

In this thesis, we adopt  $\Lambda$ CDM cosmology with  $H_0 = 73 \text{ km s}^{-1} \text{ Mpc}^{-1}$ ,  $\Omega_M = 0.27$  and  $\Omega_\Lambda = 0.73$ , resulting in a scale of  $66.7 \text{ kpc arcmin}^{-1}$  for the redshift, 0.06 of A1795.

### 1.6.1 4C 26.42

A1795 hosts 4C 26.42 (B2 1346+26), a very luminous cD galaxy at  $z = 0.0633$ . 4C 26.42 is identified as the brightest galaxy of A1795 and is observed to have a double Z morphology. The structure of the galaxy is shown in Figure 1.4. The galaxy has a symmetric Z structure at 5 mas in VLBI C band (5 GHz) and a similar but 90° rotated reverse structure at 2'' in VLA X band (8.4 GHz). E. Liuzzo et al. 2009 suggests different origins for the two 90° changes: one at  $\sim 5 \text{ mas}$  and another one at 2'' from the nucleus. At larger scale it could be due to buoyancy effects and at smaller scales it could be due to supermassive black hole precession or peculiar gas motion. The spectrum analysis shows that the southern lobe of the source (seen in VLBI L and VLBI C band) is steeper than the northern lobe which can be explained by the interaction of the galaxy with ICM [11].

## 1.7 Motivation

The formation of galaxy clusters is a very energetic process. A galaxy cluster consists of ICM, magnetic fields, relativistic particles, etc which involve a lot of physical processes. The study of these physical properties adds to the current knowledge of astrophysics. Galaxy clusters also give information about the structure and the evolution of the universe over large length scales and time scales. Since they can be detected at multiple

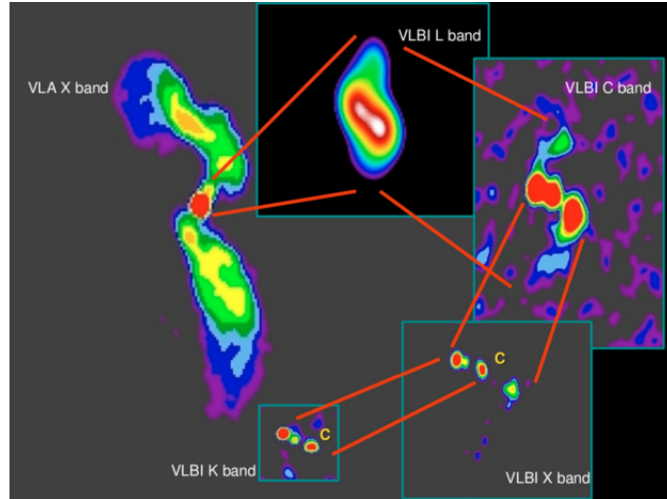


Figure 1.4: *Parsec scale structure of 4C 26.42. Here, C is the core for 4C 26.42 [11]*

---

$RA_{J2000}$	$13h\ 48m\ 52.5s$
$DEC_{J2000}$	$+26^\circ\ 35'\ 34''$
Major Axis	$11.8''(\sim 13kpc)$
Minor Axis	$5.5''(\sim 6kpc)$
Position Angle	$12.14^\circ$
redshift	0.06
Luminosity Distance	$258\ Mpc$

---

Table 1.1: *Properties of 4C 26.42 (BCG)*

wavelengths and at high redshifts, galaxy clusters act as important tools to study cosmology and to understand the evolution of the large scale structure of the universe.

Galaxy clusters are detected and studied at multiple wavelengths from X-ray to Radio. The hot gas from the galaxies and ICM emit X-ray through thermal bremsstrahlung and the relativistic electrons in magnetic fields emit synchrotron radiation detected at radio wavelengths. The analysis of the radio spectrum of the source gives information about its evolution. Moreover, the age of the source can be estimated from the curvature of the spectrum and the break frequency. Hence, the study of the spectrum of radio sources becomes important to understand the history and evolution of the cluster.

Mini-halos are diffuse radio sources whose emission encompasses the central bright radio galaxy of the cluster. Understanding this emission is important but given its proximity to a bright radio source, it is difficult to detect mini-halos. The emission is due to turbulence in the ICM and several theories have been proposed to explain the origin of this turbulence. One such theories is the sloshing motion of the gas in the cool core of relaxed clusters which generates sufficient turbulence to re-accelerate the relativistic electrons. However, the origin of mini-halos and their relation to the core is not fully understood given the small number of mini-halos detected. A total of 21 mini-halos have been detected as given by Giacintucci et al. (2013) [9]. Hence, it becomes important to detect mini-halos to understand their properties.

A candidate mini-halo detection is claimed by Giacintucci et al. (2013) [9] at  $1.4 \text{ GHz}$ . Analysis at other frequencies is needed to confirm its presence. In this thesis, we undertake the task of detecting the mini-halo at  $610 \text{ MHz}$  and  $235 \text{ MHz}$ . Along with the mini-halo, we also discuss the brightest cluster galaxy, 4C 26.42. The radio spectrum of the galaxy can give information on the energetics and lifetime of the galaxy. In this thesis, we estimate the age, equipartition magnetic field and total energy of the relativistic electrons in the galaxy from the spectrum.

# Chapter 2

## Observations

### 2.1 Radio Telescope

The antenna of a radio telescope receives the radio signals from the source.

#### Noise in the system

If power  $P$  is received at the antenna terminals, the temperature of the antenna is defined as:

$$T_A = \frac{P}{k} \quad (2.1)$$

where  $k$  is the Boltzmann constant.

The total system temperature  $T_{sys}$  is sum of  $T_{sky}$ ,  $T_R$  and  $T_{ground}$  where  $T_{sky}$  is the contribution from the sky brightness,  $T_R$  is the receiver temperature and  $T_{ground}$  is the contribution from the ground and surrounding hills.

#### Signal to Noise Ratio

The rms fluctuations for a signal of bandwidth  $\Delta\nu$  integrated over a time  $\tau$  is  $T_{sys}/\sqrt{\Delta\nu\tau}$ . The signal received is  $GS$  where  $G$  is the gain pattern of the antenna (the transmitting or receiving pattern of the antenna) and  $S$  is the flux density of the source. The signal to noise ratio (SNR) is defined as:

$$SNR = \frac{GS\sqrt{\Delta\nu\tau}}{T_{sys}} \quad (2.2)$$

## Antenna reception Pattern

The effective aperture of an antenna is defined as:

$$A(\nu, \theta, \phi) = \frac{\text{Power density available at the terminals}}{\text{Flux density incident on the antenna}} \quad (2.3)$$

The reception pattern of the antenna is:

$$A(\nu, \theta, \phi) = \frac{A(\nu, \theta, \phi)}{A_o} \quad (2.4)$$

where  $A_o$  is the response at the center of the main lobe of  $A(\nu, \theta, \phi)$

The effective power received by the antenna is:

$$P = A(\nu, \theta, \phi) I(\nu, \theta, \phi) \Delta\nu \Delta\Omega \quad (2.5)$$

where  $I(\nu, \theta, \phi)$  is the intensity of the emission,  $\Delta\nu$  is the bandwidth and  $\Delta\Omega$  is the solid angle. The reception pattern of an antenna is shown in Figure 2.1. The half power beam width  $\theta_{HPBW} \sim \lambda/D$  where  $D$  is the diameter of the telescope.

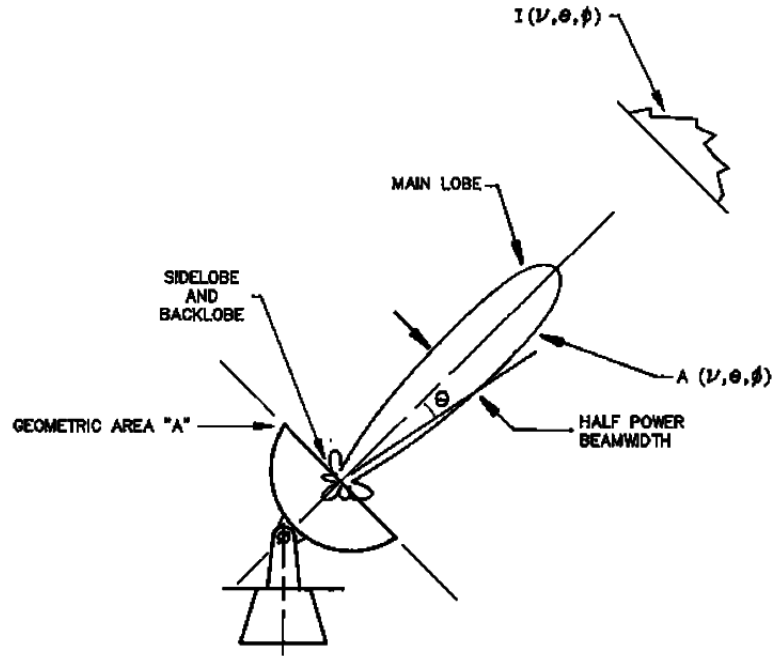


Figure 2.1: *The reception pattern of an antenna [16]*

## 2.2 Radio Interferometry

Rayleigh criterion gives the resolution of a telescope to be

$$\theta \sim \lambda/D \quad (2.6)$$

where  $D$  is the aperture size. To obtain high resolutions at meter wavelengths (radio), the aperture has to be very large (hundreds of kilometers). Building a single dish telescope of this size is not practical. Hence, the technique of aperture synthesis is used which is based on the principle of interferometer. The visibilities (correlations of the electric fields at two antennas) are related to the intensity of the source through a Fourier transform (See Section 3.2). At any instant, for an interferometer of  $N$  antennas there are  $N(N - 1)/2$  visibilities.

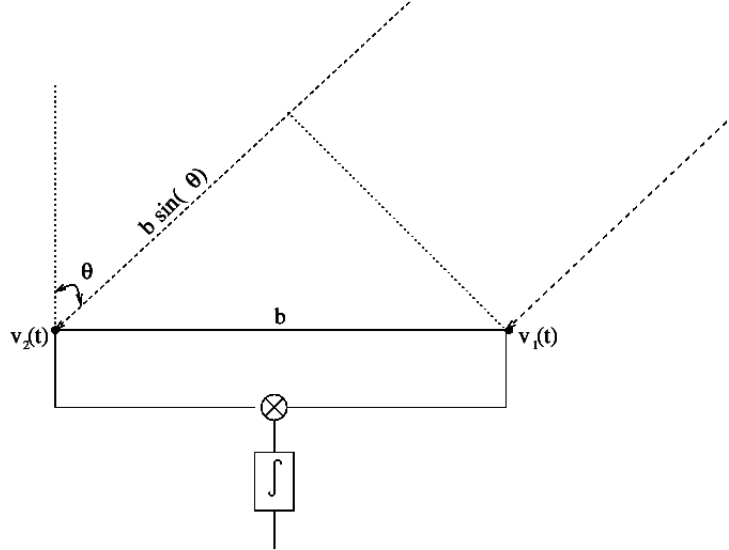


Figure 2.2: Two element interferometer

The averaged output (over time  $T$ ) of the multiplier for  $V_1(t) = \cos(2\pi\nu t)$  and  $V_2(t) = \cos(2\pi\nu(t - \tau_g))$  where  $\tau_g = b \sin(\theta)$  is:

$$r(\tau_g) = \frac{1}{T} \int_{t-T/2}^{t+T/2} \cos(2\pi\nu t) \cos(2\pi\nu(t - \tau_g)) dt \quad (2.7)$$

$$= \cos(2\pi\nu\tau_g) \quad (2.8)$$

For an interferometer observing with a bandwidth  $\Delta\nu$ , the response is given by:

$$r(\tau_g) = \frac{1}{\Delta\nu} \int_{\nu-\Delta\nu/2}^{\nu+\Delta\nu/2} \cos(2\pi\nu\tau_g) d\nu \quad (2.9)$$

	Frequency ( $MHz$ )	
	235	610
Primary Beam (arc min)	114±5	43±3
Total System Temperature ( $K$ ) ( $T_R + T_{sky} + T_{ground}$ )	237	102
Synthesized Beam (arcsec)	13	5
Largest Detectable Source(arcmin)	44	17
Frequency Range ( $MHz$ )	236-244	580-640

Table 2.1: *GMRT Parameters*

$$= \cos(2\pi\nu\tau_g) \left[ \frac{\sin(\pi\Delta\nu\tau_g)}{\pi\Delta\nu\tau_g} \right] \quad (2.10)$$

The minimum size of the sources for them to be distinguished by interferometer is

$$\Delta\theta \lesssim \lambda/b \quad (2.11)$$

where  $b$  is the baseline of the interferometer. Greater the  $b$ , higher the resolution.

For an interferometer of  $N$  antennas,

$$SNR = \frac{GS\sqrt{\Delta\nu\tau}}{\sqrt{T_{sys}N(N-1)}} \quad (2.12)$$

## 2.3 GMRT

The Giant Meterwave Radio Telescope (GMRT) is a low frequency telescope situated at about 80  $km$  from Pune. It consists of 30 telescopes each having a diameter of 45  $m$ . GMRT has a Y-shaped configuration with the central region spread over 1  $km^2$  and the longest baseline is about 25  $km$ . The array configuration is shown in Figure 2.3. GMRT operates at 153, 233, 325, 610 and 1420  $MHz$  with a bandwidth of 32  $MHz$ . GMRT parameters are given in Table 2.1. In this thesis, we analysed GMRT data at 610  $MHz$  and 235  $MHz$ .



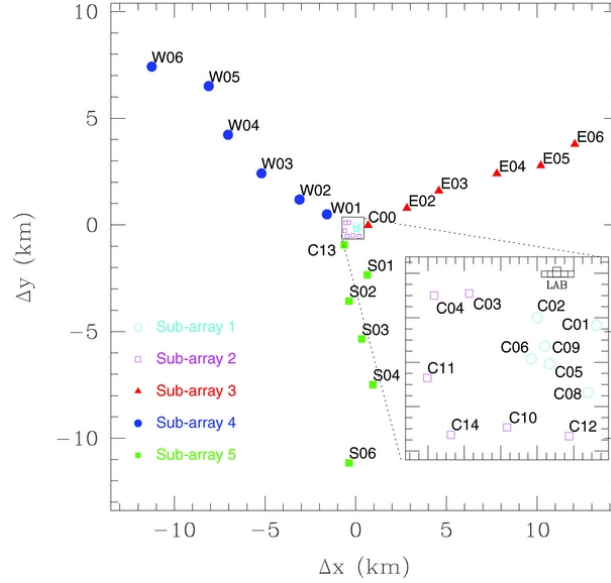


Figure 2.3: GMRT array (Figure 3 from N. D. R. Bhat et al. 2013 *ApJS* 206 2.)

## 2.4 Observations at 610 MHz and 235 MHz

The source A1795 was observed using the GMRT on 19 November, 2011. Observations at 610 MHz and 235 MHz are considered in this thesis. The source A1795 at 610 MHz and 235 MHz is observed for a total of about 3.5 hours. The calibrator source, 3C286 (used as both primary and secondary calibrator) is observed in the beginning and at the end of the observation. The source is observed for about 30 minutes followed by the calibrator source which is observed for about 8 minutes. A total of 7 scans for the source and 8 scans for the calibrator source are taken.

Table 2.2 gives the scan number and the timings during which the observations of the source were taken.

The observations are taken at reference frequencies 629 MHz and 253 MHz with a bandwidth of 32 MHz and 16 MHz respectively. A total of 512 channels are considered with a channel resolution of 65 kHz at both 610 MHz and 235 MHz.

Scan	IST
1	5:23:38 - 5:54:30
3	6:01:45 - 6:32:37
5	6:40:08 - 7:10:44
7	7:18:31 - 7:49:07
9	7:56:38 - 8:27:31
11	8:35:18 - 9:05:54
13	9:13:41 - 9:44:17

Table 2.2: *IST when the source A1795 was observed*

# Chapter 3

## Data Analysis

### 3.1 Flagging and Calibration

The process of removing the bad data is called flagging. The obviously bad data has to be removed from the raw data before proceeding with the calibration as any corruption in the input visibilities while estimating antenna gains result in incorrect gains.

The observed visibilities have to be corrected to obtain the true visibilities.

$$V_{i,j}^{obs}(\nu, t) = V_{i,j}^{true}(\nu, t)G_i(t)G_j(t)B_{i,j}(\nu, t) \quad (3.1)$$

where  $G_i(t)$  and  $G_j(t)$  are the gains of antenna  $i$  and  $j$  and  $B_{i,j}(\nu, t)$  is the frequency dependent gain.

Calibration is a process of determining these complex gains to obtain the true visibilities for the source of interest.

$G(t)$  is a complex quantity with amplitude and phase as functions of time. In order to determine these gains, a bright source whose flux density is known and is constant is observed (primary calibrator). The amplitude gains for the antennas are estimated from the true and observed visibilities of the calibrator source which can then be applied to the observed visibilities of the source of interest. Several factors like the tropospheric effects, the electronic gains, voltage pattern, etc contribute to the antenna gain. A calibrator source near the source of interest is also used to incorporate the tropospheric effects in the estimation of gains and to determine the phases. This is the secondary calibrator.

A bright source near the source of interest can be used both as primary and secondary calibrator.

$B(\nu, t)$  is the complex frequency gain of the antennas with amplitude and phase as functions of frequency.  $B$  could be constant over the length of observation or it could show a slow dependence on time. A bright unresolved sources with a good signal to noise ratio per frequency channel is to be considered as a bandpass calibrator.

In the observations of A1795 at 610  $MHz$  and 235  $MHz$ , 3C286 is used as primary, secondary and bandpass calibrator. 3C286 is a Seyfert 1 Galaxy (very luminous) with RA 13  $h$  31  $m$  08.28811  $s$ , DEC +30° 30' 32.9600" and a redshift of 0.8493. The flux densities of 3C286 at GMRT 610  $MHz$  and 235  $MHz$  are 21.2  $Jy$  and 28.1  $Jy$  respectively (Chandra P. et al. The Astrophysical Journal, 612(2), 974)

The FLAGCAL program is used for flagging and calibration of the data analysed during this project. The raw visibilities are given as input to this program which outputs the flagged and calibrated data. This output can directly be used for imaging. The basic principle used to identify bad data in this algorithm is that the true visibilities vary slowly and frequently in time compared to the noise in the data. The calibration is done after flagging the obviously bad data. This is followed by further flagging and calibration by specifying more stringent conditions [5].

### **610 MHz**

The flux density of the calibrator 3C286 is set to 21.22  $Jy$ . The fraction of data flagged is given in Table 3.1. The output of FLAGCAL for each scan at 610  $MHz$  is given in Table 3.3.

### **235 MHz**

The flux density of the calibrator 3C286 is set to 29.62  $Jy$ . The fraction of data flagged is given in Table 3.2. The output of FLAGCAL for each scan at 235  $MHz$  is given in Table 3.3.

Source	Total visibilities	Fraction flagged
3C286	32707584	0.12
A1795	145207296	0.14

Table 3.1: *Total amount of data flagged at 610 MHz*

Source	Total visibilities	Fraction flagged
3C286	12495600	0.09
A1795	56721600	0.11

Table 3.2: *Total amount of data flagged at 235 MHz*

## 3.2 Imaging

I referred to *Synthesis Imaging in Radio Astronomy II* [16] to write this section on imaging. The detailed explanation can be found in the same.

The radio antennas collect the electromagnetic fields from the source of interest. One assumption is that the source of radiation is very far off from the observer. Hence, we can assume that the radiation we receive is from the surface of a celestial sphere of radius  $|R|$  which is far from both the observer and the source and which has no radiation within it. The electric field on this sphere is denoted by  $E_\nu(R)$  and the electric field received by us at  $r$  from an element of surface area  $dS$  on the sphere is given by:

$$E_\nu(r) = \int E_\nu(R) \frac{e^{2\pi i \nu |R-r|/c}}{|R-r|} dS \quad (3.2)$$

The observed intensity of the source is related to the spatial correlation as:

$$V_\nu(r_1, r_2) \approx \int I_\nu(s) e^{-2\pi i \nu s \cdot (r_1 - r_2)/c} d\Omega \quad (3.3)$$

where

$V_\nu(r_1, r_2) = \langle E_\nu(r_1) E_\nu^*(r_2) \rangle$  is the spatial correlation of the electric fields at observer positions  $r_1$  and  $r_2$

$s$  is the unit vector:  $R/|R|$

$d\Omega = dS/|R|^2$  is the differential solid angle and

Scan	Source	Mean Visibility Amplitude( $Jy$ )		Flagged Fraction	
		610 $MHz$	235 $MHz$	610 $MHz$	235 $MHz$
0	3C286	$2.4467e + 01$	$2.2418e + 01$	0.14	0.10
1	A1795	$1.5098e + 00$	$4.9290e + 00$	0.15	0.09
2	3C286	$2.3842e + 01$	$2.2545e + 01$	0.14	0.09
3	A1795	$1.4753e + 00$	$4.8797e + 00$	0.17	0.09
4	3C286	$2.4433e + 01$	$2.3071e + 01$	0.14	0.12
5	A1795	$1.5141e + 00$	$4.8193e + 00$	0.17	0.11
6	3C286	$2.3464e + 01$	$2.2728e + 01$	0.14	0.11
7	A1795	$1.5888e + 00$	$5.0609e + 00$	0.17	0.14
8	3C286	$2.3723e + 01$	$2.1735e + 01$	0.14	0.10
9	A1795	$1.6563e + 00$	$4.9923e + 00$	0.10	0.13
10	3C286	$2.3130e + 01$	$2.2254e + 01$	0.09	0.08
11	A1795	$1.7295e + 00$	$5.1134e + 00$	0.10	0.11
12	3C286	$2.2530e + 01$	$2.2459e + 01$	0.09	0.09
13	A1795	$1.8230e + 00$	$5.4391e + 00$	0.12	0.13
14	3C286	$2.1255e + 01$	$2.1166e + 01$	0.08	0.07

Table 3.3: *Fraction of data flagged in each scan at 610 MHz and 235 MHz*

$I_\nu(s) = |R|^2 \langle |E_\nu(s)|^2 \rangle$  is the observed intensity.

The spatial correlation function and the intensity are related by a Fourier transform by considering one of the two assumptions explained below. A coordinate system in which the separation term in the spatial auto correlation function is defined in terms of the wavelength of the electrical signal is used. In this coordinate system,  $r_1 - r_2 = \lambda(u, v, w)$  and the components of the unit vector  $s$  are  $(l, m, n \equiv \sqrt{1 - l^2 - m^2})$  (Figure 3.1).

### Assumptions:

1.) Consider the measurements are made in a plane i.e.  $w \equiv 0$ . In this case,

$$V_\nu(u, v, w \equiv 0) = \int \int I_\nu(l, m) \frac{e^{-2\pi i(ul+vm)}}{\sqrt{1-l^2-m^2}} dl dm \quad (3.4)$$

The intensity of the source is obtained by inverting this fourier transform.

2.) Consider the radiation comes from a small portion in the sky which can be approximated to a plane. In other words,  $s = s_o + \sigma$  and  $s_o$  perpendicular to  $\sigma$  where  $s_o = (0, 0, 1)$  is the phase tracking centre. In this case,

$$V_\nu(u, v) = \frac{V'_\nu(u, v, w)}{e^{-2\pi i w}} = \int \int I_\nu(l, m) e^{-2\pi i(ul+vm)} dl dm \quad (3.5)$$

### Dirty image

The  $u - v$  space is not sampled everywhere or even uniformly. The sampling function,  $S_\nu(u, v)$  is a dirac delta function at the positions where there is data. The image thus obtained is dirty and is given by:

$$I_\nu^D = \int \int V_\nu(u, v) S_\nu(u, v) e^{2\pi i(ul+vm)} du dv \quad (3.6)$$

This equation can also be written as a convolution of the actual image  $I_\nu$  and the point spread function (dirty beam)  $B$  i.e.  $I_\nu^D = I_\nu * B$  where

$$B = \int \int S_\nu(u, v) e^{2\pi i(ul+vm)} du dv \quad (3.7)$$

### 3.2.1 CLEAN algorithm

The CLEAN algorithm deconvolves the dirty image  $I_\nu^D$  to obtain the clean image  $I_\nu$ . In this algorithm, the brightest sources are selected and the dirty beam multiplied by

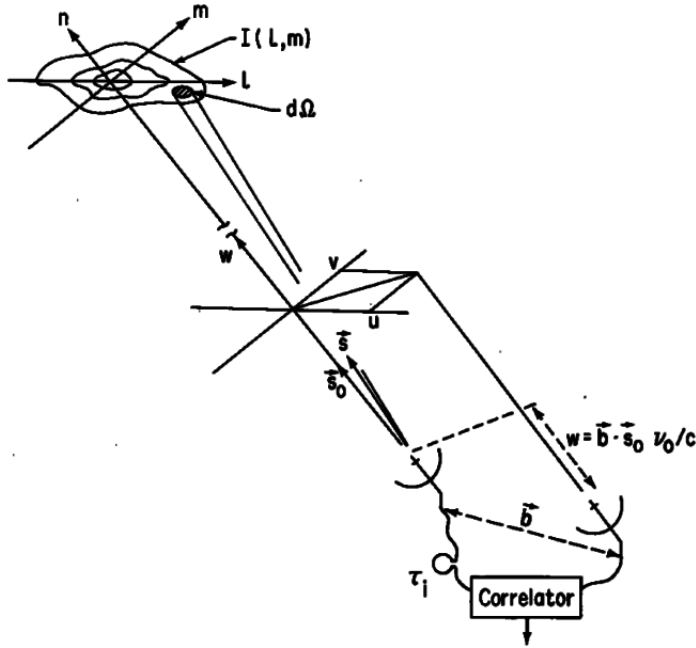


Figure 3.1: *Coordinate System [16]*

the peak intensity (of the bright source) and a loop gain factor (a damping factor) is subtracted from the dirty image at the positions of the bright sources. A residual image is left after subtraction. The positions and magnitudes of the subtracted sources is noted down. A CLEAN beam which is usually an elliptical gaussian fitted to the central lobe of the dirty beam is convolved with the bright sources. The residual image is added to the CLEAN image (which contains the convolved bright sources at their positions) to give a model image. Self-calibration is a method like CLEAN. In self-calibration, the complex gains ( $G_i(t), G_j(t)$ ) are calculated from the model image. The corrected visibilities ( $V_{i,j}^{corr}(t)$ ) are obtained from the initial visibilities ( $V_{i,j}^{obs}(t)$ ) as follows:

$$V_{i,j}^{corr}(t) = \frac{V_{i,j}^{obs}}{G_i(t)G_j(t)} \quad (3.8)$$

A new model image is produced from the corrected visibilities. This process is repeated to get the final clean image.

### 3.2.2 Weighting

The sampling function is given weights to control the sidelobes of the dirty beam or to improve the noise in the image. The weighted sampling function  $W(u, v)$  and the corresponding  $M$  weighted visibilities  $V^W(u, v)$  ( $M$  is of the same order of  $N^2$  of a  $N \times N$



grid) are given below:

$$W(u, v) = \sum_{k=1}^M R_k T_k D_k \delta(u - u_k, v - v_k) \quad (3.9)$$

$$V^W(u, v) = \sum_{k=1}^M R_k T_k D_k \delta(u - u_k, v - v_k) V'(u_k, v_k) \quad (3.10)$$

$R_k$  is the weighting function which indicates the reliability of the  $k^{th}$  visibility. It may depend on the system temperature, integration time, bandwidth, etc.

$T_k$  is a tapering function which is used to downweight the data as a function of distance from the centre of  $(u, v)$  coverage. This reduces the sidelobes and increases the beam width (which is required to detect extended emission). A Gaussian tapering function is usually considered which is of the form  $T(r) = e^{-r^2/2\sigma^2}$ . The half power beam width is defined as  $\theta_{HPBW} = 0.37/\sigma$  where  $\theta$  is in radians and  $\sigma$  is in wavelength. To detect weak sources within the extended emission, the visibilities near the centre are downweighted by using a relevant tapering function.

$D_k$  is a density weighting function which gives weights to the visibilities depending on the density of data points ( $N_s(k)$ ) within a width  $s$  (which could be the radius of a circle or the side of a square around the  $k^{th}$  visibility). A density function could give a natural or a uniform weighting to the visibilities. In case of natural weighting,  $D_k = 1$  which gives equal weighting to all the points. Since there are more number of visibilities at short spacings, natural weighting gives more weight to datapoints near short spacings. This results in a high signal to noise ratio but gives a broad beam width which is not ideal in detecting weak point sources. In uniform weighting,  $D_k = 1/N_s(k)$  which de-emphasizes the visibilities at short spacings (as there are more number of data points at low spacings). This results in a uniform  $(u, v)$  coverage with a higher resolution. The signal to noise ratio is less than that obtained by natural weighting. A robust weighting can produce both uniform and natural weighting which can be specified by giving a robust parameter. A robust parameter of  $-2$  is close to uniform weighting and a robust parameter of  $+2$  is close to natural weighting. Robust weighting gives a sensitivity and resolution inbetween uniform and natural weighting.

### 3.2.3 Polyhedron Imaging

The visibilities are given as:

$$V(u, v, w) = \int \int I(l, m) B(l, m) e^{-2\pi i(ul+vm+w\sqrt{1-l^2-m^2})} \frac{dldm}{\sqrt{1-l^2-m^2}} \quad (3.11)$$

This can be transformed into 2-D a fourier relation by assuming a small field of view i.e.  $l^2 + m^2 \ll 1$ . However, this approximation is not valid in case of wide field imaging. Polyhedron imaging is a technique used for wide field imaging.

The 3-D fourier inversion of  $V(u, v, w)$  (defined as the image volume  $I(l, m, n)$ ) is related to the 2-D sky brightness distribution  $I(l, m)$  as:

$$I(l, m, n) = \frac{I(l, m)\delta(\sqrt{1-l^2-m^2}-n)}{\sqrt{1-l^2-m^2}} \quad (3.12)$$

The sources of emission lie on the surface of the sphere of radius  $n = \sqrt{1-l^2-m^2}$ . The image volume and it's relation to the 2-D surface brightness is shown in Figure 3.2

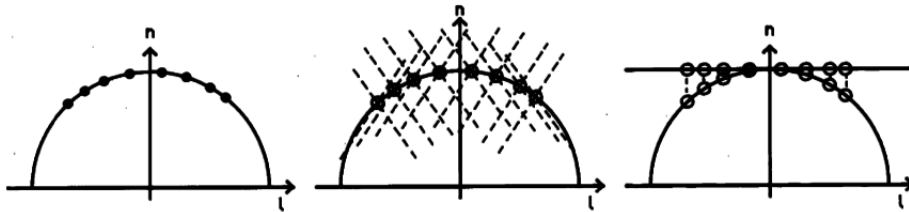


Figure 3.2: *The left figure shows the image (sources on unit sphere  $l, m = 0, n = \sqrt{1-l^2-m^2}$ ) obtained from 3-D fourier transform of visibilities. The figure in the middle shows the convolution of the sources with the 3-D dirty beam. The figure on the right shows the sources which after deconvolution are convolved with clean beams. The 2-D image is obtained by projection of the 3-D image on the sphere onto a tangent plane. [16]*

The emission from phase centre and the sources close to it can be approximated to be lying in the tangent plane. In polyhedron imaging for wide field, the celestial sphere is approximated by a number of tangent planes (fields) as shown in Figure 3.3. The 2-D small field approximation is valid in each of these tangent planes.

The number of tangent planes to be considered is given by:

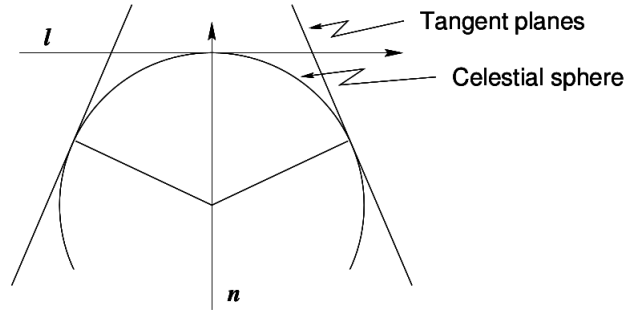


Figure 3.3: *Polyhedron Imaging* [16]

$$N_{poly} = \frac{2B\theta^2}{\lambda} \quad (3.13)$$

where  $B$  is the longest baseline and  $\theta$  is the size of the image considered. If the full image is to be taken into account, then  $\theta = \lambda/D$  where  $D$  is the diameter of the antenna dish.

The theoretical number of fields in the full image at  $610 \text{ MHz}$  and  $235 \text{ MHz}$  is calculated using Eq. 3.13.

At  $610 \text{ MHz}$ , taking  $\lambda \sim 0.5 \text{ m}$ ,  $D = 45 \text{ m}$  and  $B = 24 \text{ km}$  (for GMRT),  $N_{poly} \sim 12$ .

At  $235 \text{ MHz}$ , taking  $\lambda \sim 1.28 \text{ m}$ ,  $D = 45 \text{ m}$  and  $B = 24 \text{ km}$  (for GMRT),  $N_{poly} \sim 30$ .

### 3.2.4 610 MHz

The calibrated and flagged data is considered for imaging. A total of 40 channels with an initial frequency of  $612 \text{ MHz}$  and channel width of  $650 \text{ kHz}$  is considered. The task *SETFC* on this data gives a cellsize of  $1''$  and an image size of 1024 pixels with 49 fields within  $4^\circ$ .

The final image (by giving a robust value of 0) is produced after 5 phase calibrations and 1 amplitude& phase (A& P) calibration using the tasks *IMAGR* and *CALIB*. The first two images are cleaned interactively while a threshold limit of 3 to  $5\sigma$  is given for other images. All the images are produced by polyhedron imaging using the 49 fields. To get an image of only point sources (R-2), the task *IMAGR* is run by giving a robust value of  $-2$  on the visibilities obtained after A& P selfcalibration. Similarly, an image (R+2) is produced with a robust value of  $+2$  to get an image with diffuse sources. R-2 is

Image	resolution(")	Position angle( $^{\circ}$ )	rms( $mJy/beam$ )
Final image (R=0)	$7.4 \times 4.9$	31.94	0.14
R+2	$10 \times 8.3$	34.89	0.26
R - 2	$6 \times 3.8$	28.42	0.15
Subtracted Image	$10 \times 8.3$	34.89	0.2

Table 3.4: *610 MHz*

convolved with and subtracted from the R+2 to get an image which contains only diffuse emission.

Radio emission is detected at  $1.4 \text{ GHz}$  in a  $2' \times 2'$  region around the BCG [9]. Hence, in order to detect the mini-halo at  $610 \text{ MHz}$ , we obtain the flux density of this region at  $610 \text{ MHz}$ . The flux density from a region of  $\sim 120'' \times 110''$  ( $\sim 70 \text{ kpc}$  radius) around the central galaxy in the subtracted image is  $\sim 18 \text{ mJy}$ .

The resolution, position angle and rms values for the  $610 \text{ MHz}$  images are given in Table 3.4.

### 3.2.5 235 MHz

The calibrated and flagged data is averaged to 16 channels with a channel width of  $650 \text{ kHz}$ . 19 fields within  $2^{\circ}$  radius are considered for polyhedron imaging.

After an interactive clean on the first image, the final image is produced after 4 phase and 2 A& P self calibrations by giving limits on the threshold flux density. Images are produced with robust values of 0, +2 (R+2) and  $-2$  (R-2). R-2 image is convolved with and subtracted from R+2. We detected negative flux density values at the positions of the bright sources which indicates that the subtraction has not worked properly. Hence, we do not consider the subtracted image at  $235 \text{ MHz}$  in our analysis to detect the mini-halo.

The resolution, position angle and rms values for the  $235 \text{ MHz}$  images are given in Table 3.5.

Image	resolution(")	Position angle( $^{\circ}$ )	rms( $mJy/beam$ )
Final image(R=0)	$15.16 \times 12.97$	-57.84	1.8
R+2	$19.27 \times 17.76$	81.64	3.3
R - 2	$12.62 \times 10.67$	-35.35	2.2

Table 3.5: *235 MHz*

# Chapter 4

## Results

### 4.1 Radio Images of BCG

#### 4.1.1 610 MHz

The overlay of R-2 610 MHz radio contours on the Xray CHANDRA and Optical DSS is given in Figure 4.1. The resolution of the radio image is  $6'' \times 3.8''$ , in p.a.  $-28.42^\circ$  and rms noise is  $1\sigma \sim 0.15$  mJy.

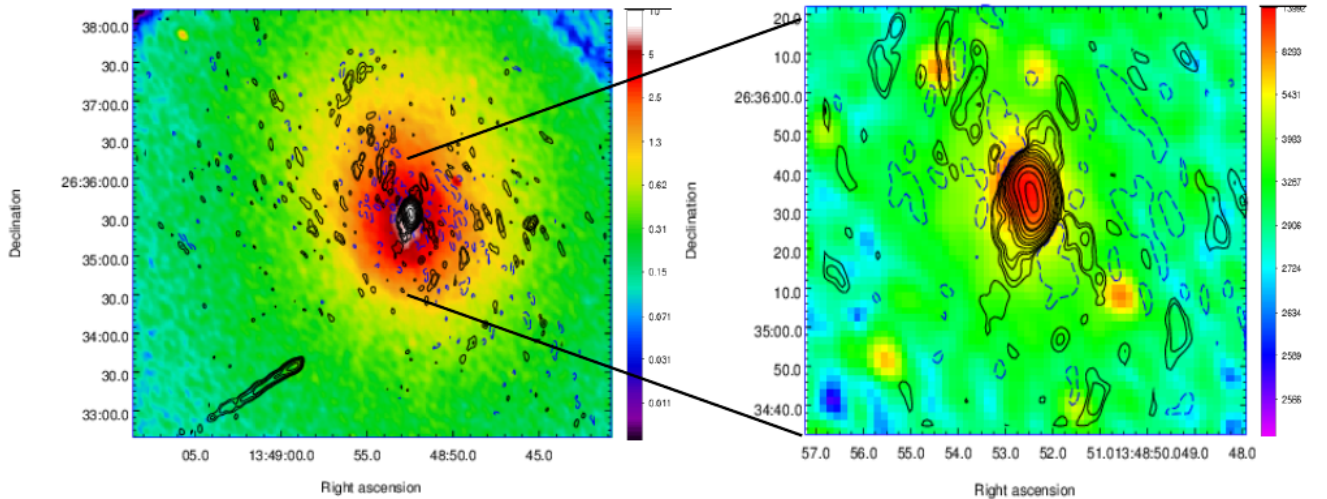


Figure 4.1: *i) Left: Radio contours of R-2 610 MHz at  $-3$  (blue dashed),  $3, 5, 10, 15, 30, 60, 100, 200, 400, 800, 1000, 2000, 4000 \times \sigma$  (black) on Xray Chandra colour image in  $0.5-4$  keV band. *ii) Right: The BCG is zoomed in. R-2 610 MHz radio contours of the galaxy  $-5$  (blue dashed),  $3, 5, 10, 15, 30, 60, 100, 200, 400, 800, 1000, 2000 \times \sigma$  (black) on the DSS Optical colour image.**

### 4.1.2 235 MHz

The overlay of R-2 235  $MHz$  radio contours on the Xray CHANDRA and Optical DSS is given in Figure 4.2. The resolution of the radio image is  $12.6'' \times 10.7''$ , in p.a.  $-35.35^\circ$  and rms noise is  $1\sigma \sim 2.2 \text{ mJy}$ .

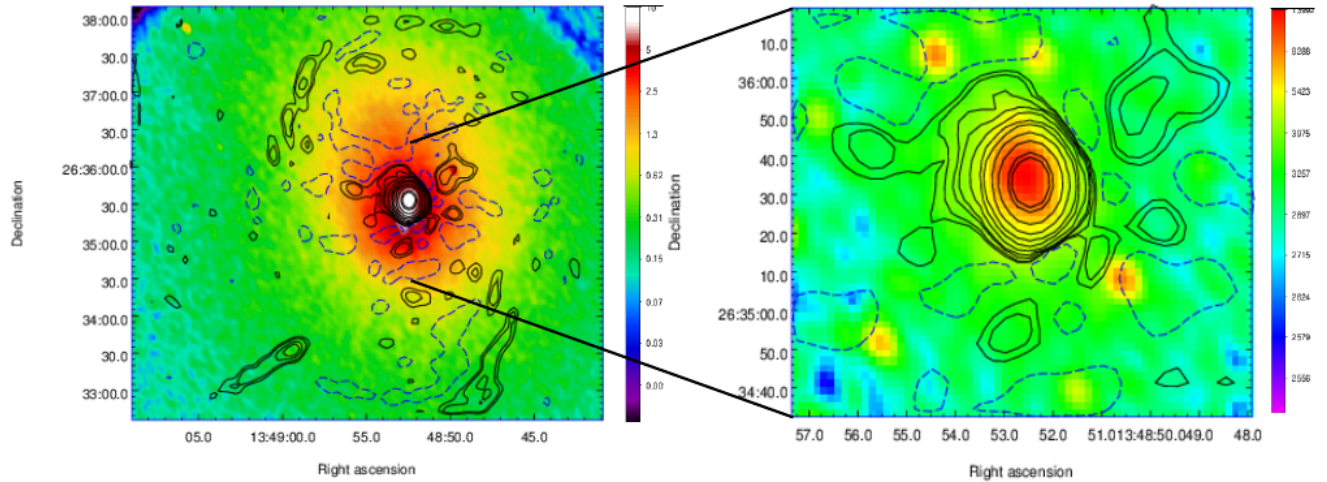


Figure 4.2: *i) Left: Radio contours of R-2 235 MHz at -3 (blue dashed), 3,5,10,15,30,60,100,200,400,800,1000,2000,4000  $\times \sigma$  (black) on Xray Chandra colour image in 0.5-4 keV band. ii) Right: The BCG is zoomed in. R-2 235 MHz radio contours of the galaxy -5 (blue dashed), 3,5,10,15,30,60,100,200,400,800,1000,2000  $\times \sigma$  (black) on the DSS Optical colour image.*

## 4.2 Spectrum of BCG

The spectrum of the BCG, 4C 26.42 is obtained using the flux density values from 74  $MHz$  to 43.34  $GHz$  (Table 4.1). Figure 4.3 shows the spectrum of the BCG:  $\log(S_\nu)$  versus  $\log(\nu)$  plotted with a least square fit.

The flux density values at 610  $MHz$  and 235  $MHz$  are estimated from the R+2 GMRT images using JMFIT. The error on the flux densities is estimated from the flux densities of 3C286 at different scans. The variance is calculated and the error with respect to the mean is  $\sim 10\%$  at both 610  $MHz$  and 235  $MHz$ . This error percentage is considered for the flux densities of the source. Values at the remaining frequencies are taken from the Nasa Extragalactic Database (NED) ([2], [6], [10]). Since the flux density of the whole

Frequency(MHz)	S(mJy)	Error in S(mJy)	Telescope	Resolution(")	PA( $^{\circ}$ )
43340	12.24	$\pm 0.67$	VLA DnC	$2 \times 3$	-
22460	21.79	$\pm 1.02$	VLA DnC	$2 \times 3$	-
8460	110.74	$\pm 0.84$	VLA DnC	$8 \times 4$	-
4860	234.6	$\pm 0.5$	VLA DnC	$8 \times 13$	-
1400	917	$\pm 46$	VLA B	$5 \times 5$	-
610	2199.3	$\pm 220$	GMRT	$7.4 \times 4.9$	-31.94
235	4903.2	$\pm 490$	GMRT	$15 \times 13$	-57.84
74	10870	$\pm 1090$	VLA BnA	80	40.5

Table 4.1: *Col 1:Frequency, Col 2:flux density, Col 3:Errors in flux density, Col 4: Telescope array configuration, Col 5: Synthesized beam and Col 6: Position angle*

galaxy is to be considered to get the spectrum, one has to make sure that the image is not resolved out. Hence, we selected the flux density values obtained from VLA configurations taking resolution into consideration. We considered arc second resolution and not milliarc second resolutions.

### 4.3 Break frequency

From Figure 4.3, we observe that the spectrum curves between 1 GHz and 3 GHz. To obtain the frequency at which the spectrum steepens, we fit a linear least square fit for the frequencies 74 MHz - 1.4 GHz and 4.86 GHz - 43.34 GHz as shown in Figure 4.4. The point of intersection is the break frequency  $\sim 2$  GHz.

From the plot, we can estimate the slopes using  $S_{\nu} \propto \nu^{-\alpha}$ .

$$\alpha_{74MHz}^{1.4GHz} \equiv \alpha_1 = 0.83 \pm 0.05$$



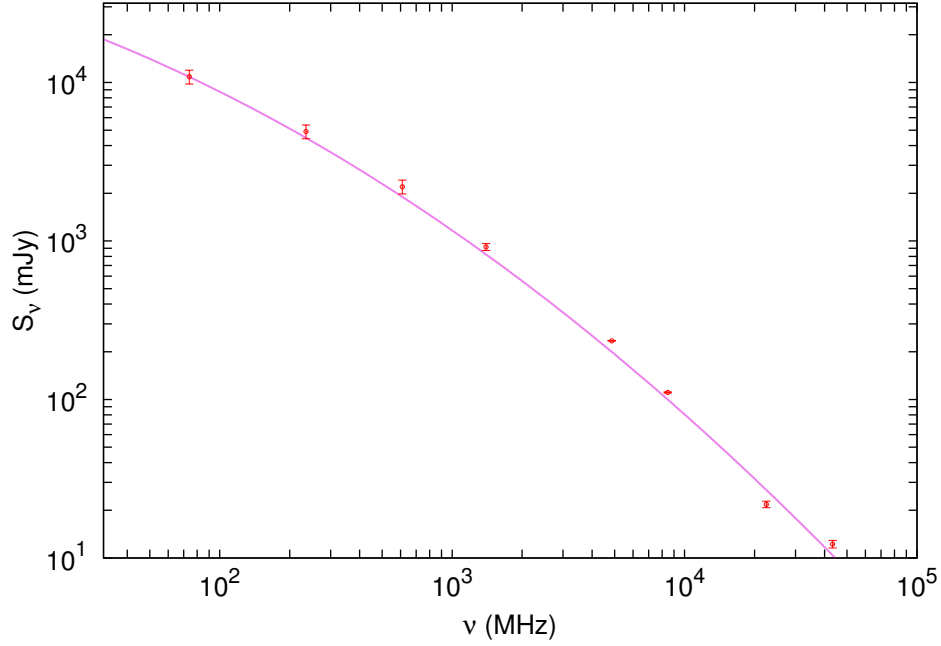


Figure 4.3: *Spectrum of the BCG.*

*The spectrum follows the curve:  $\log S_\nu = -0.14(\log \nu)^2 - 0.16(\log \nu) + 4.8$ .*

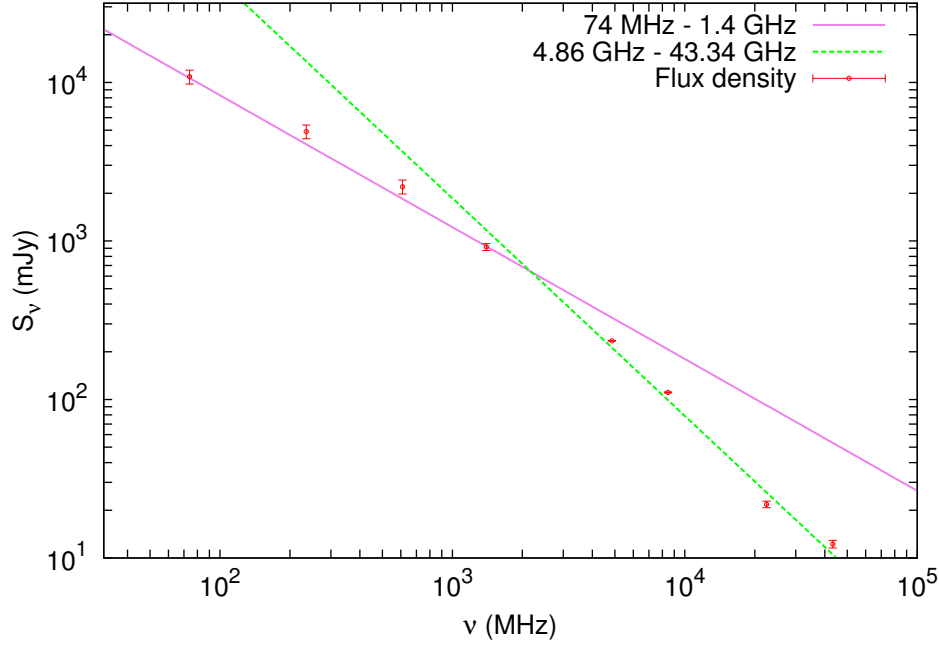
$$\alpha_{4.86GHz}^{43.34GHz} \equiv \alpha_2 = 1.37 \pm 0.14$$

## 4.4 Magnetic field from Equipartition of Energy

I referred to *Galactic and Extragalactic radio astronomy* [17] for the derivation discussed in this section.

We assume the following while calculating the magnetic field using equipartition of energy.

1. Synchrotron Emission is only from relativistic electrons.
2. Isotropization of pitch angle of the relativistic electron in magnetic field.
3. The source is approximated to a cylinder.



74 MHz-1.4 GHz follows the equation  $\log S_\nu = -0.83 \log \nu + 5.6$

4.86 GHz-43.34 GHz follows  $\log S_\nu = -1.37 \log \nu + 7.4..$

Figure 4.4: *Spectrum of the BCG with the break frequency.*

The Synchrotron power emitted by a relativistic electron in CGS is given by:

$$P \equiv \frac{dE}{dt} = 2\sigma\gamma^2\beta^2c \frac{(B \sin \theta)^2}{8\pi} \quad (4.1)$$

$B$  is the Magnetic field in  $\mu G$

$E$  is the energy of the electrons in *erg*.

Thomson Cross section ( $\sigma$ ) for electron =  $6.65 \times 10^{-25}$  cm and  $\beta^2 \sim 1$  for  $\gamma \gg 1$  gives

$$P \equiv \frac{dE}{dt} = 2.368 \times 10^{-3} E^2 (B \sin \theta)^2 \quad (4.2)$$

The total energy of the relativistic electrons is given by

$$E_e = \int_{E_1}^{E_2} N(E) dE \quad (4.3)$$

The distribution of electrons  $N(E)$  is

$$N(E) = KE^{-p} \quad (4.4)$$

where  $K$  is a constant and  $p$  is the index of electron distribution.

Therefore Eq.4.3 becomes

$$E_e = K \int_{E_1}^{E_2} E^{1-p} dE \quad (4.5)$$

We know that luminosity can be written as

$$L = \int_{E_1}^{E_2} N(E) \left( \frac{dE}{dt} \right) dE \quad (4.6)$$

using Eq.4.2 and Eq.4.4, Eq.4.6 can be written as

$$L = 2.368 \times 10^{-3} K (B \sin \theta)^2 \int_{E_1}^{E_2} E^{2-p} dE \quad (4.7)$$

Eliminating  $K$  from Eq.4.5 and Eq.4.7 and on integration, we get

$$E_e = \frac{L(B \sin \theta)^2 (3-p) (E_2^{(2-p)} - E_1^{(2-p)})}{2.368 \times 10^{-3} (2-p) (E_2^{(3-p)} - E_1^{(3-p)})} \quad (4.8)$$

Now,  $E$  can be written in terms of the frequency  $\nu$  as

$$E = 1.595 \times 10^{-10} \nu^{1/2} (B \sin \theta)^{-1/2} \quad (4.9)$$

Using Eq.4.9 in Eq.4.8, we get

$$E_e = \frac{L(B \sin \theta)^{-3/2} (3-p) (\nu_2^{(2-p)/2} - \nu_1^{(2-p)/2})}{3.78 \times 10^{-13} (2-p) (\nu_2^{(3-p)/2} - \nu_1^{(3-p)/2})} \quad (4.10)$$

We know that the spectral index of the particle distribution  $p$  ( $N(E) = KE^{-p}$ ) and the spectral index of the radio spectrum  $\alpha$  ( $S_\nu \propto \nu^{-\alpha}$ ) are related as

$$\alpha = \frac{(p-1)}{2} \quad (4.11)$$

Since the spectrum of the galaxy is curved, we considered an equivalent  $\alpha$  which gives the same  $\int_{\nu_1}^{\nu_2} S_\nu d\nu$  as that of the curved spectrum. This equivalent  $\alpha = 1.07$  which gives  $p = 3.14$ .

Considering this value for  $p$  and taking the average of  $(\sin \theta)^{-3/2}$  over all angles (isotropization of pitch angles), we get

$$E_e = 0.2681 \times 10^9 LB^{-3/2} \quad (4.12)$$

The energy in the magnetic field of the galaxy is given by

$$E_B = \frac{B^2}{8\pi} V \quad (4.13)$$

where the volume of the galaxy ( $V$ ) =  $1.121 \times 10^{67} \text{ cm}^3$  gives

$$E_B = 4.46 \times 10^{65} B^2 \quad (4.14)$$

The total energy  $E_T$  is

$$E_T = E_e + E_B \quad (4.15)$$

Minimizing  $E_T$  with respect to  $B$  gives the Equipartition condition

$$\frac{E_e}{E_B} = \frac{4}{3} \quad (4.16)$$

Using Eq.4.12 and Eq.4.14 in Eq.4.16 with a luminosity  $L = 6 \times 10^{41} \text{ ergsec}^{-1}$ , we get,

$$\text{Minimum Magnetic Field } B_{min} \sim 36 \mu G$$

$$\text{Energy of relativistic electrons } E_e \sim 8 \times 10^{56} \text{ erg}$$

$$\text{Magnetic Field Energy } E_B \sim 6 \times 10^{56} \text{ erg}$$

$$\text{The Total Energy } E_T \sim 10^{57} \text{ erg}$$

The corresponding values for Cygnus A which is a bright radio galaxy are given below:

$$\text{Luminosity } L = 6 \times 10^{44} \text{ erg sec}^{-1}$$

$$\text{Minimum Magnetic Field } B_{min} \sim 0.4 \mu G$$

$$\text{The Total Energy } E_T \sim 3 \times 10^{59} \text{ erg}$$

## 4.5 Age of relativistic electrons

The time since the process of emission started or the age of the relativistic electrons is estimated from the break frequency as given by Slee, O. B., et al.(2001) [15].

We consider continuous injection of relativistic electrons with a constant injection rate and isotropization of the pitch angle distribution to estimate the age.

The age is given by:

$$t = \frac{1060B^{1/2}[(1+z)\nu_b]^{-1/2}}{[B^2 + B_{IC}^2]} \quad (4.17)$$

where,

$t$  is in  $Myr$

$\nu_b$  is the break frequency in  $GHz$

$B$  is the minimum magnetic field from equipartition of energy in  $\mu G$

$B_{IC}$  is the effective Inverse Compton magnetic field given by

$$B_{IC} = \sqrt{\frac{2}{3}}B_{CMB} \quad (4.18)$$

where the CMB radiation field is

$$B_{CMB} = 3.25(1+z)^2\mu G \quad (4.19)$$

For

$\nu_b = 2 GHz$  (Figure 4.4),  $B = 36 \mu G$  and  $z = 0.06$ ,

we get the age  $t \sim 3.4 Myr$  (estimated using Equation 4.17).

From the age, it can be said that this galaxy is young. However, this age is calculated using the equipartition magnetic field which is only an approximation. We further estimate the age of the relativistic electrons by considering magnetic fields which deviate from the equipartition magnetic field.

By considering a magnetic field which is 10 times the equipartition magnetic field i.e. by considering  $B = 360 \mu G$ , the age of the relativistic electrons is estimated to be  $\sim 0.1 Myr$ .

By considering  $B = 3.6 \mu G$ , the age is estimated to be  $\sim 63 Myr$  or  $\sim 0.06 Gyr$ .

This galaxy can be considered to be young given that the estimated age of our milkyway is  $\sim 10 - 13 Gyr$ .

# Chapter 5

## Discussion

### 5.1 Diffuse Emission

#### 5.1.1 Upper limit on flux density of mini-halo

Mini-halos are diffuse radio sources of the size  $\sim 100$  *kpc* in the centre of galaxy clusters. The spectrum of a mini-halo is steep with the average spectral index  $\alpha$  being 1 ( $S_\nu \propto \nu^{-\alpha}$ ). A candidate mini-halo is claimed to be present at 1.4 *GHz* in the galaxy cluster A1795 [9]. We give an upper limit to the flux density of the mini-halo at 610 *MHz*. Only 21 mini-halos have been detected till now and it is important to detect more to understand their properties and origin.

An integrated flux density of  $\sim 18$  *mJy* is detected at 610 *MHz* from a region which is roughly the size of a mini-halo ( $\sim 1'$  radius which corresponds  $\sim 70$  *kpc* radius) in the centre of the subtracted image (R-2 subtracted from R+2). However, we believe that this flux density is the percentage left over in the image due to incomplete subtraction from R+2 image. About 1% of flux density is left over in the image at the positions of the bright sources. This is probably due to calibration errors which are not taken care of. Hence, the integrated flux density of 18 *mJy* in the subtracted image can not be attributed to the mini-halo. The percentage left over at the positions of bright sources in the subtracted image are given in Table 5.1.

An integrated flux density of  $85 \pm 5$  *mJy* at 1.4 *GHz* of the mini-halo is claimed by Giacintucci et al. (2013) [9]. By considering the spectral index of the mini-halo to be 1 (average spectral index is 1 for diffuse emission), the integrated flux density at 610 *MHz*

Pixel values around bright sources				
BLC	TRC	R+2	Subtracted image	% left
3315, 3891	3359, 3927	53.7	0.53	1
3527, 4247	3563, 4283	47.63	0.62	1
3627, 4071	3663, 4107	41.3	2.7	7
4615, 5047	4659, 5087	61.48	7.3	12

Table 5.1: *Col 3: Flux density (mJy) in R+2 image, Col 4: Flux density (mJy) in the subtracted image, Col 5: % of flux density left in the subtracted image. Here, 1 pixel corresponds to 1''*

should be  $\sim 160$  mJy. However, we detected an integrated flux density of  $\sim 18$  mJy from the central region of the subtracted image. This is about 10 times lower than the expected value. The integrated flux density from the same region in the R+2 image is  $\sim 2$  Jy which shows that  $\sim 1\%$  of flux density (from the BCG in R+2) is left over in the subtracted image due to incomplete subtraction. This number agrees with the percentage flux left at the positions of other bright sources. Hence, we believe the flux density detected in the subtracted image is the left over flux density and not the flux density of the mini-halo. We give an upperlimit of 18 mJy for the mini-halo in A1795.

### 5.1.2 Radio Power of mini-halo at 1.4 GHz

Based on literature, the radio power of 20 mini-halos at 1.4 GHz is known. The  $P_{1.4GHz}$  (radio power at 1.4 GHz) values of the 20 mini-halos are given in Table 5.2.

The average radio power of a mini-halo from these values is  $\sim 4 \times 10^{24}$  W Hz<sup>-1</sup>.

Using the upper limit of 18 mJy at 610 MHz, the flux density at 1.4 GHz is  $\sim 8$  mJy (by considering a spectral index of 1). The radio power at 1.4 GHz is estimated using this flux density limit. The radio power of a source is related to its flux density as:

$$P_{1.4GHz} = 4\pi D_L^2 S_{1.4GHz} \quad (5.1)$$

Galaxy Cluster	$S_{MH1.4GHz}$ (mJy)	$P_{MH1.4GHz}$ ( $10^{24}WHz^{-1}$ )	Radius (kpc)	$S_{BCG1.4GHz}$ (mJy)	$P_{BCG1.4GHz}$ ( $10^{24}WHz^{-1}$ )
MACSJ0159.8-0849	$2.4 \pm 0.2$	$1.4 \pm 0.14$	90	$35 \pm 1.8$	$20.3 \pm 0.1$
MACSJ0329.6-0211	$3.8 \pm 0.4$	$2.84 \pm 0.3$	70	$3.8 \pm 0.2$	$2.8 \pm 0.1$
A478	$16.6 \pm 3$	$0.32 \pm 0.06$	160	$31.0 \pm 1.6$	$0.60 \pm 0.03$
ZwC13146	$\sim 5.2$	$\sim 1.39$	90	$\sim 3.3$	$\sim 0.8$
RXJ1532.9+3021	$7.5 \pm 0.4$	$3.35 \pm 0.17$	100	$15.7 \pm 0.8$	$7 \pm 0.4$
A2204	$8.6 \pm 0.9$	$0.54 \pm 0.05$	50	$58.9 \pm 2.9$	$3.7 \pm 0.2$
ZwCl 1742.1+3306	$13.8 \pm 0.8$	$0.20 \pm 0.01$	40	$68.8 \pm 3.4$	$0.97 \pm 0.05$
MACS J1931.82634	$47.9 \pm 2.8$	$20.0 \pm 1.2$	100	$11.6 \pm 0.05$	$4.9 \pm 0.2$
Perseus	$3020 \pm 153$	$2.18 \pm 0.11$	130	-	$13.4 \pm 0.1$
A1835	$6.1 \pm 1.3$	$1.19 \pm 0.25$	240	-	$6.3 \pm 0.3$
Ophiuchus	$83.4 \pm 6.6$	$0.15 \pm 0.02$	250	-	$0.064 \pm 0.003$
A2029	$19.5 \pm 2.5$	$0.28 \pm 0.04$	270	-	$7.4 \pm 0.4$
A2390	$28.3 \pm 4.3$	$4.46 \pm 0.67$	250	-	$33.2 \pm 1.7$
RBS 797	$5.2 \pm 0.6$	$2.20 \pm 0.24$	120	-	$7.6 \pm 0.4$
RXC J1504.10248	$20.0 \pm 1.0$	$2.70 \pm 0.14$	140	-	$5.7 \pm 0.3$
RX J1347.51145	$34.1 \pm 2.3$	$25.59 \pm 1.79$	320	-	$22.7 \pm 1.1$
RX J1720.1+2638	$72.0 \pm 4.4$	$5.33 \pm 0.32$	140	-	$0.50 \pm 0.02$
MS 1455.0+2232	$8.5 \pm 1.1$	$1.75 \pm 0.23$	120	-	$0.96 \pm 0.05$
2A 0335+096	$21.1 \pm 2.1$	$0.059 \pm 0.006$	70	-	$0.058 \pm 0.003$
A2626	$18 \pm 1.8$	$0.14 \pm 0.01$	30	-	$0.129 \pm 0.006$

Table 5.2: Col 1: Cluster name, Col 2: Flux density of the mini-halo in the cluster at 1.4 GHz, Col 3: Radio power of the mini-halo at 1.4 GHz, Col 4: Radius of the mini-halo, Col 5: Flux density of the BGC at 1.4 GHz, Col 6: Radio power of the BCG at 1.4 GHz [9].



where  $D_L$  is the luminosity distance of the source and  $S_{1.4GHz}$  is its flux density at 1.4 GHz.

By considering  $D_L = 258 \text{ Mpc}$  and  $S_{1.4GHz} = 8 \text{ mJy}$  for the mini-halo, the upper limit on the radio power of the mini-halo  $P_{1.4GHz} \sim 6 \times 10^{22} \text{ W Hz}^{-1}$ .

The upper limit on  $P_{1.4GHz}$  of the mini-halo in A1795 is  $\sim 100$  times lower than the average  $P_{1.4GHz}$  obtained from other mini-halos. This is one of the indications that there might not be a mini-halo in A1795.

### 5.1.3 Implications

A possible detection of mini-halo in A1795 at 1.4GHz has been claimed by Giacintucci et al. (2013) [9]. The reasons for believing so are given below:

A1795 is a relaxed cool core cluster and X-ray studies of this cool core indicate the presence of a cold front at  $\sim 70''$  south of the centre in the CHANDRA image [12]. The sloshing motion within the cold front could create enough turbulence for the formation of a mini-halo. It is also suggested that the emission from mini-halo in the southern portion may be constricted by the cold front [9].

We propose the possible reasons why we could not detect the mini-halo at 610 MHz.

One reason could be that the emission observed by Giacintucci et al. (2013) in the radio images at 1.4 GHz is the emission from the BCG and not the mini-halo. Given the proximity of a mini-halo to a bright source, a careful subtraction of the emission from the BCG has to be done to observe the diffuse emission. We believe that the flux density of the mini-halo at 1.4 GHz is over estimated. At 1.4 GHz, the flux density of the BCG and a nearby point source obtained from VLA B configuration (resolution of  $5''$  at 1.4 GHz) is subtracted from the total integrated flux density obtained from the low resolution VLA C configuration (resolution of  $18.7'' \times 16.0''$ ). It is possible that the total flux density of the BCG was not recovered by VLA B configuration given that the BCG is an extended source and VLA B configuration gives a high resolution. This might have left some flux density from the BCG which could have been attributed to the mini-halo flux density.

In our analysis at 610 MHz, we subtracted the image with point sources (R-2 image with a resolution of  $6'' \times 3.8''$ ) from the low resolution image (R+2 with a resolution of  $10'' \times 8.3''$ ). This is done to subtract the point sources from the low resolution image and

not just subtract the flux density of point sources. This is a more rigorous way to make sure that most of the contribution from the BCG is subtracted out. In spite of careful subtraction of point sources, we did not detect a mini-halo in A1795.

Assuming that the flux density detected at 1.4  $GHz$  is the actual flux density of the mini-halo, one reason for the non-detection at 610  $MHz$  could be that the spectrum of the mini-halo is flat (with a spectral index  $< 1$ ). However, in this case, even a spectral index of 0 gives a flux density of  $\sim 85 mJy$  at 610  $MHz$  which is still above the upper limit of detection ( $\sim 18 mJy$  at 610  $MHz$ ). Hence, this possibility can be ruled out.

This non-detection of the diffuse emission could also mean that there is no mini-halo in the galaxy cluster A1795. It is also possible that there is a mini-halo but it can be detected only below the upper limit mentioned in section 5.1.1.

## 5.2 Brightest Cluster Galaxy

The flux density of the BCG, 4C 26.42 at 1.4  $GHz$  ( $S_{BCG1.4GHz}$ ) in A1795 is  $917 \pm 46 mJy$  (estimated using VLA B array) and its radio power  $P_{BCG1.4GHz}$  is  $8.5 \pm 0.4 \times 10^{24} W Hz^{-1}$  [9]. The flux densities and radio powers of other BCGs at 1.4  $GHz$  are given in Table 5.2. The radio power value of the BCG in A1795 agrees with the radio power values of other BCGs.

### 5.2.1 Magnetic field and Total Energy

A magnetic field strength of  $36 \mu G$  and total energy (electron energy + magnetic field energy) of  $\sim 10^{57} ergs$  is obtained for the BCG in A1795 using equipartition of energy between the particle energy density and the magnetic field energy. The minimum total energy and the mean magnetic field strength ( $B$ ) required for synchrotron emission in galaxies are given in Table 5.3. The mean magnetic field strength required for synchrotron emission in a galaxy ranges from  $10^{-7} - 10^{-4} G$  and the total energy ranges from  $10^{54} - 10^{59} ergs$ . Our estimate of the minimum energy magnetic field ( $36 \mu G$ ) and the total energy ( $10^{57} ergs$ ) lies within the respective ranges.

Radio Source	Total Energy (ergs)	Mean $B$ (gauss)
M31	$2 \times 10^{55}$	$8 \times 10^{-7}$
Magellanic clouds	$3 \times 10^{54}$	$1 \times 10^{-6}$
NGC 4038-39	$2 \times 10^{56}$	$2 \times 10^{-6}$
NGC 1068	$3 \times 10^{55}$	$2 \times 10^{-5}$
NGC 5128(central region)	$3 \times 10^{56}$	$2 \times 10^{-5}$
NGC 5128(halo)	$5 \times 10^{58}$	$1 \times 10^{-6}$
NGC 1316(central region)	$2 \times 10^{56}$	$2 \times 10^{-5}$
NGC 1316(halo)	$2 \times 10^{58}$	$1 \times 10^{-6}$
NGC 4486(central source)	$2 \times 10^{57}$	$1 \times 10^{-5}$
NGC 1275	$1 \times 10^{57}$	$2 \times 10^{-5}$
NGC 6166	$1 \times 10^{57}$	$3 \times 10^{-5}$
Hydra A	$1 \times 10^{58}$	$8 \times 10^{-5}$
Cygnus A	$3 \times 10^{59}$	$4 \times 10^{-5}$
Coma Cluster	$3 \times 10^{59}$	$2 \times 10^{-7}$

Table 5.3: *Col 1: Radio Source, Col 2: Minimum total energy (electron energy + magnetic field energy) required for synchrotron emission, Col 3: Mean magnetic field strength required for synchrotron emission. The values are obtained by considering minimum energy assumption (equipartition magnetic field) [3].*

## 5.2.2 Spectrum

From Figure 4.4, we get the break frequency and the spectral indices of the power laws ( $S_\nu = \nu^{-\alpha}$ ) before and after the break frequency.

The break frequency  $\nu_{br} \sim 2GHz$

The spectral index before the break frequency  $\alpha_1 = 0.83 \pm 0.05$

The spectral index after the break frequency  $\alpha_2 = 1.37 \pm 0.14$

The relation between  $\alpha_1$  and  $\alpha_2$  is:

$$\alpha_2 - \alpha_1 = 0.54 \pm 0.15 \sim 0.5 \quad (5.2)$$

The relation between  $\alpha_1$  and  $\alpha_2$  shows that either the CI model or the KGJP model (assuming isotropization of pitch angle) fits the data (details in Section 1.4).

If KGJP model is considered then:

$\nu_{br}$  is the first break frequency i.e. the break frequency of the first electron population injected.

$\alpha_1 = \alpha_{inj}$  for  $\nu < \nu_{br}$  and

$\alpha_2 = \alpha_{inj} + 0.5$  for  $\nu_{br} < \nu < \nu'_{br}$

The age of the relativistic electrons is estimated using the formula given by Slee, O. B., et al.(2001) [15] by considering the KGJP model.

## 5.2.3 Implications

The curvature of the spectrum and the presence of a break frequency clearly indicates synchrotron losses (refer to Section 1.4) in the BCG. The sharp cutoff in the spectrum of the BCG could be due to the high magnetic field strength in the BCG. This galaxy is in the cool core of the galaxy cluster A1795. A cool core has a high density of particles compared to the surrounding intracluster medium. This confines the expansion of the lobes of the galaxy which inturn result in higher magnetic field strength. Higher the magnetic field, greater are the synchrotron losses which can lead to a sharp cutoff in the spectrum.

Data at higher frequencies is required to detect the second break frequency ( $\nu'_{br}$ ) if it is present. The detection of  $\nu'_{br}$  could confirm the KGJP model of spectral aging in the BCG from which one can estimate the duration of injection and the duration of the relic phase.

In the absence of a second break frequency, one can assume the CI model of spectral aging for the galaxy.

# References

- [1] Abell, George O., Harold G. Corwin Jr, and Ronald P. Olowin. "A catalog of rich clusters of galaxies." *The Astrophysical Journal Supplement Series* 70 (1989): 1-138.
- [2] Becker, Robert H., Richard L. White, and David J. Helfand. The FIRST survey: faint images of the radio sky at twenty centimeters. *The Astrophysical Journal* 450 (1995): 559.
- [3] Burbidge, G. R. "Estimates of the Total Energy in Particles and Magnetic Field in the Non-Thermal Radio Sources." *The Astrophysical Journal* 129 (1959): 849-852.
- [4] Carilli, C. L., et al. "Multifrequency radio observations of Cygnus A-Spectral aging in powerful radio galaxies." *The Astrophysical Journal* 383 (1991): 554-573.
- [5] Chengalur, J. N. NCRA Technical Report, NCRA/COM/001 (April 2013).
- [6] Cohen, A. S., et al. The VLA low-frequency sky survey. *The Astronomical Journal* 134.3 (2007): 1245.
- [7] Feretti, Luigina, et al. "Clusters of galaxies: observational properties of the diffuse radio emission." *The Astronomy and Astrophysics Review* 20.1 (2012): 1-60.
- [8] Ghizzardi, Simona, Mariachiara Rossetti, and Silvano Molendi. "Cold fronts in galaxy clusters." arXiv preprint arXiv:1003.1051 (2010).
- [9] Giacintucci, Simona, et al. "New detections of radio minihalos in cool cores of galaxy clusters." arXiv preprint arXiv:1311.5248 (2013).
- [10] Lin, Yen-Ting, et al. Spectral energy distribution of radio sources in nearby clusters of galaxies: implications for Sunyaev-Zeldovich effect surveys. *The Astrophysical Journal* 694.2 (2009): 992.

- [11] Liuzzo, E., et al. "The parsec-scale properties of the radio galaxy 4C 26.42 in the dense cooling core cluster A1795." arXiv preprint arXiv:0905.3453 (2009).
- [12] Markevitch, M., A. Vikhlinin, and P. Mazzotta. "Nonhydrostatic gas in the core of the relaxed galaxy cluster A1795." *The Astrophysical Journal Letters* 562.2 (2001): L153.
- [13] Markevitch, Maxim, and Alexey Vikhlinin. "Shocks and cold fronts in galaxy clusters." *Physics Reports* 443.1 (2007): 1-53.
- [14] Rybicki George B., and Alan P. Lightman. *Radiative processes in astrophysics*. John Wiley and Sons, 1979.
- [15] Slee, O. B., et al. "Four extreme relic radio sources in clusters of galaxies." *The Astronomical Journal* 122.3 (2001): 1172.
- [16] Taylor, Greg B., Chris Luke Carilli, and Richard A. Perley. "Synthesis imaging in radio astronomy II." *Synthesis Imaging in Radio Astronomy II*. Vol. 180. 1999.
- [17] Verschuur, Gerrit L., and Kenneth I. Kellermann. *Galactic and extra-galactic radio astronomy*. Berlin: Springer, 1988, 2nd ed., edited by Verschuur, Gerrit L.; Kellermann, Kenneth I. 1 (1988).